

RESEARCH PAPER

CHARACTERIZATION OF CHROMIUM NITRIDE PRECIPITATION IN THE HEAT AFFECTED ZONE OF THE SUPERDUPLEX STAINLESS STEEL UNS S32750: AN EXPERIMENTAL AND NUMERICAL ANALYSIS

Paolo Ferro¹, Alberto Fabrizi¹, Jan-Olof Nilsson², Franco Bonollo¹

¹Department of Engineering and Management, University of Padova, Stradella San Nicola 3, 36100 Vicenza, Italy

²JON Materials Consulting, Sjökatan 2, 651 71, Arvika, Sweden

*Corresponding author: paolo.ferro@unipd.it tel.: +39 0444 998769 Department of Engineering and Management, University of Padova, Stradella San Nicola 3, 36100 Vicenza, Italy

Received: 16.03.2021

Accepted: 29.04.2021

ABSTRACT

It is well known that pitting corrosion resistance of duplex and superduplex stainless steels strongly depends on microstructural characteristics such as ferrite/austenite proportion, presence of intermetallic phases and elemental partitioning between the austenite and ferrite phases. In particular, during the welding operation, very fine chromium nitrides may precipitate within ferrite grains of the heat affected zone drastically reducing the corrosion resistance of welded joints of duplex and super duplex stainless steels. However, due to their small size and low distribution, analyzing the chemical composition and crystallography of chromium nitrides is quite difficult and only a restricted number of advanced techniques of investigation may discriminate their signal from the surrounding matrix. This work is aimed at supporting the microstructural characterization of a welded joint of a superduplex stainless steel by means of a field-emission gun scanning electron microscope. Sub-micron chromium nitride precipitates, identified within the ferritic grains of the heat affected zone, are recognized to be the main reason for the reduced pitting corrosion resistance of the analyzed welded joints. The results are supported by a multi-pass welding process numerical simulation aimed at estimating the cooling rates promoting chromium nitride precipitation in the heat affected zone. The model is proven to work well and be a useful design instrument for assessing optimal welding process parameters.

Keywords: Super duplex stainless steels, Chromium nitride, microstructure, thermal model, multi-pass welding; numerical simulation

INTRODUCTION

Duplex (DSS) and superduplex (SDSS) stainless steels are increasingly used in aggressive environments thanks to their outstanding combination of mechanical strength, corrosion resistance in various types of environments and weldability. For ensuring such excellent combination of properties, it is essential to maintain a ferrite-austenite ratio close to 50:50 and avoid the precipitation of undesired phases such as secondary austenite (γ_2), chromium nitrides, carbides, sigma (σ) and chi (χ) phases [1-12].

Unfortunately, the thermal cycles induced by welding operations alter the optimized microstructure of the parent metal. The fusion zone (FZ) and the heat-affected zone (HAZ) are generally characterized by an unbalanced ratio between ferrite and austenite because of the high temperatures reached and the high cooling rates characterizing the welding process. Since the peak temperature in the HAZ is much higher than the upper limit of phase balance between δ -ferrite and austenite, most of the γ islands in the prior duplex structure dissolve into the δ -ferrite matrix during the heating period. During cooling, in the temperature range between 1300 and 800 °C, austenite starts to re-precipitate, both in the FZ and HAZ, mainly at the ferrite grain boundaries due to higher free energy of these locations. Because of the high cooling rate of the weld metal, the ferrite-austenite transformation is inhibited, and less austenite will be formed compared with the parent material (PM). Even if very

low heat input may prevent the precipitation of brittle intermetallic phases such as σ or χ , it may lead to high ferrite contents and intense nitride precipitation [13-15]. A proper filler metal, the chemical composition of which is rich in Ni, may partially restore the balance between primary austenite and δ ferrite, but unfortunately it does not solve the problem of chromium nitrides precipitation in HAZ.

In fact, it is widely reported that chromium nitride precipitation can occur within ferrite grains in different duplex grades during the welding process due to the rapid cooling rate [16-22]. Indeed, austenite grains transform to ferrite in the high temperature heat affected zone (HAZ) and the high cooling rates partially inhibit austenite re-transformation resulting in a nitrogen supersaturated ferrite which is enriched in Cr. Consequently, chromium nitride particles precipitate in ferrite grains, mainly intragranular (Fig. 1), but also along the ferrite/austenite interfaces and ferrite subgrain boundaries.

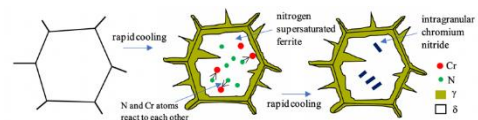


Fig. 1 Schematic of chromium nitride precipitation in HAZ

In multi-pass welding a cooperative precipitation mechanism of Cr-N and secondary austenite (γ_2) could take place [23], as well. As a matter of fact, a chromium-rich and nitrogen-poor zone forms around chromium nitride, which promotes γ_2 nucleation.

Chromium nitrides are found to drastically reduce the mechanical and corrosion properties of DSS and SDSS [24, 25] and this is the main reason why the welding engineer should know the chromium nitrides mechanism formation, the techniques available to detect them, and take care in selecting process parameters in order to prevent their existence. However, due to their small size and low distribution, the chemical and crystallographic analysis of chromium nitrides is quite difficult and only a limited number of advanced techniques may discriminate their signal from that of the surrounding matrix. In the aforementioned works, the chemical analysis of Cr-N is generally omitted or deduced. For instance, Zhang et al. [26] pointed out that after electrically etching in oxalic acid solution, some pits were observed, indicating the appearance of chromium nitride.

Only in few investigations of DSS and SDSS, transmission electron microscopy (TEM) coupled with electron diffraction were carried out to clearly identify the composition and crystallography of chromium nitrides precipitated during thermal treatments simulating welding processes [16, 22, 27].

Anyway, in practical experience, the precipitation of chromium nitrides in welded DSS and SDSS occurs in some ferrite grains confined to the thin HAZ layer resulting in a cumbersome TEM sample preparation using standard procedures.

Using Field Emission Gun-Scanning Electron Microscopy (FEG-SEM) with a significantly smaller beam and an increased current density compared to traditional SEMs, higher resolution micrographs can be collected, and consequently beneficial results are achieved also in chemical microanalysis by an Energy Dispersive Spectrometer (EDS) attached to the microscope.

In the present work, in FEG-SEM the EDS-linescan technique was used to determine the elemental composition of sub-micron precipitates in the HAZ of a welded UNS S32750 SDSS and a Cr-N particle has been identified. This work is aimed both at supporting the microstructural investigation carried out in a previous work on the same SDSS welded joints [7] and to develop a numerical model of the multi-pass welding process useful to predict the conditions under which chromium nitrides precipitate. The numerical model should result in a design tool useful to the welding engineer to predict the conditions promoting Cr-N precipitation as well as the optimal process parameters to avoid them.

MATERIAL AND METHODS

Material, geometry and welding process parameters

Butt-welded joints made of SDSS thick plates (15 mm), type UNS S32750 previously solution treated at 1070 °C and then quenched, were produced by submerged-arc welding (SAW) using the groove shown in Fig. 2 and process parameters collected in table 1. The heat input is obtained by using the following formula:

$$HI [kJ / mm] = h \frac{V [V] \cdot I [A]}{v [mm / s]} \quad (1.)$$

where V is the voltage, I is the amperage, v is the travel speed and h is the thermal efficiency that for SAW is approximately equal to 0.95 [28].

In table 2, the nominal chemical compositions of both parent and filler metal are summarized. It can be noted that the filler metal is enriched in nickel compared to the base material in order to contrast the high cooling rate and promote the correct balanced austenite/ferrite ratio in the FZ.

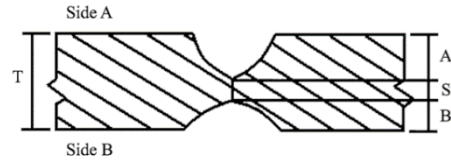


Fig. 1 Geometry of the adopted groove (T = 15 mm, A = 4 mm, S = 5 mm, B = 6 mm); figure not to scale

Metallographic examinations

For microstructure characterization, metallographic sections transverse to the weld bead were initially ground and polished using standard metallographic preparation techniques and then chemically etched with a 40% HNO₃ aqueous solution that does not attack Cr-N precipitates, as reported in Ref. [16]. The resulting microstructures were evaluated using Optical Microscopy (OM) and Field Emission Gun Scanning Electron Microscopy (FEG-SEM, Quanta 250 from Fei©) equipped with Energy Dispersive Spectroscopy (EDS, Edax©). For elemental composition of a precipitate, EDS linescan microanalysis was carried out using a probe size of about ~ 50 nm and inter-spot distance of ~ 3 nm for a dwell time of 1800 ms.

Material, geometry and welding process parameters

A thermal numerical model was developed using Sysweld® numerical code with the aim at estimating the thermal fields and cooling rates that promote precipitation of chromium nitrides. In particular, the transient analysis of welding heat transfer was simulated following the experimental welding process parameters in a finite element (FE) model with a moving heat source. The temperature history at each node is obtained by solving the heat flow balance equation:

$$-\left[\frac{\partial R_x}{\partial x} + \frac{\partial R_y}{\partial y} + \frac{\partial R_z}{\partial z} \right] + q(x,y,z,t) = \rho c \frac{\partial T(x,y,z,t)}{\partial t} \quad (2.)$$

where the rate of heat flow per unit area is denoted by R_x , R_y and R_z ; the current temperature is $T(x,y,z,t)$, the rate of internal heat generation is $q(x,y,z,t)$, c is the specific heat, ρ is the density, and t is the time. Eq. (2) can be revised by bringing Fourier's heat flow as

$$\begin{cases} R_x = -k_x \frac{\partial T}{\partial x} \\ R_y = -k_y \frac{\partial T}{\partial y} \\ R_z = -k_z \frac{\partial T}{\partial z} \end{cases} \quad (3.)$$

where k_x , k_y and k_z are the alloy thermal conductivity in the three directions x , y and z , respectively.

Due to temperature-dependent material properties (k and c), the associated material behavior was considered to be nonlinear. Now, by substituting Eqs. (3) into Eq. (2), the differential governing heat conduction equation can be rewritten as:

$$\rho c \frac{\partial T}{\partial t} = \frac{\partial}{\partial x} \left[k_x \frac{\partial T}{\partial x} \right] + \frac{\partial}{\partial y} \left[k_y \frac{\partial T}{\partial y} \right] + \frac{\partial}{\partial z} \left[k_z \frac{\partial T}{\partial z} \right] + q \quad (4.)$$

The solution of Eq. (4) requires the definition of initial conditions:

$$T(x, y, z, 0) = T_0(x, y, z) \quad (5.)$$

as well as boundaries conditions:

$$k_x \frac{\partial T}{\partial x} N_x + k_y \frac{\partial T}{\partial y} N_y + k_z \frac{\partial T}{\partial z} N_z + q_c + h_c(T - T_s) + h_r(T - T_r) = 0 \quad (6.)$$

In Eq. (5), $T_0(x,y,z)$ is taken equal to the ambient temperature ($T_a = 20 \text{ }^\circ\text{C}$) or eventually the pre-heating temperature. In Eq. (6) N_x , N_y and N_z are the direction cosine of the outward projected normal to the boundary; h_c (25 W/m²K [29]) and h_r are the heat transfer coefficients of convection and radiation, respectively; T is the surface temperature of the model and T_r is the temperature of the heat source instigating radiation. The

boundary heat flux is designated by q_s . The heat transfer coefficient of radiation can be written as:

$$h_r = \sigma \varepsilon F (T^2 - T_r^2)(T + T_r) \quad (7.)$$

where σ is the Stefan Boltzmann's constant, ε is the emissivity (0.7) and F is the configuration factor.

For the sake of simplicity and with the aim at speeding up the analysis in view of its use in welding design, a 2D model was carried out considering only the transverse section of the bead, as shown in Figs. 3 and 4, and exploiting the symmetry conditions. In order to simulate the effects of multi-pass welding, the whole mesh was divided into four groups. In Fig. 2, B1, B2, B3 are the groups of elements modelling the three fusion zones, while the remaining elements belong to the parent material (PM). An elements activation/deactivation function was used to simulate the effect of deposition of filler metal during welding. For instance, during the first pass, only the elements belonging to the parent material and group B1 were activated.

Table 1 Welding process parameters

Weld layer /run	Side	Filler metal		Current		Volt range [V]		Travel speed range [cm/min]		Average heat input	
		Class	Diameter [mm]	Type	Ampere range [A]						
1	A	25 9 4 NL	2.4	DC-EP	340	360	29	31	54	56	1.09
2	A	25 9 4 NL	2.4	DC-EP	390	410	32	34	46	48	1.60
3	B	25 9 4 NL	2.4	DC-EP	540	560	39	40	38	38	3.35

Table 2 Nominal chemical compositions (wt%) of parent and filler metal

	C	Cr	Cu	Mn	Mo	N	Ni	Si	P	Co	V	Ti	Nb	W	S
Parent metal	0.018	24.8	0.32	0.79	3.85	0.27	6.92	0.22	0.025	-	-	--	-	-	0.001
Filler metal	0.014	25.12	0.096	0.45	4.04	0.228	9.6	0.39	0.014	0.085	0.047	0.005	0.01	0.01	0.0005

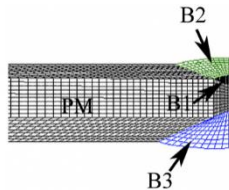


Fig. 3 Mesh of the numerical model (2427 linear finite elements) defining the groups of elements

Thermal material properties are taken as a function of temperature from Sysweld database. The heat source was modelled using a double ellipsoid power density distribution developed by Goldak et al. [30] (Eq. 8) that is commonly used in literature to model the arc heat source [31].

$$q_s(x, y, t) = \frac{6\sqrt{3}f_{1,2}Q}{\rho\sqrt{\rho abc_{1,2}}} e^{-\frac{3x^2}{a^2}} e^{-\frac{3y^2}{b^2}} e^{-\frac{3v(t-t_0)^2}{c_{1,2}^2}} \quad (8.)$$

The meaning of the symbols in Eq. (8) and their values are summarized in Tables 3 and 4.

In 2D cross section models, the heat source is thought to move over the analyzed section with a speed equal to that used in experiments as schematized in Fig. 4.

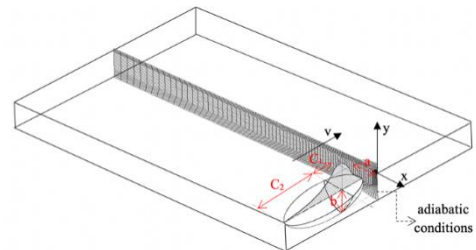


Fig. 4 Schematic of the 2D model and geometrical parameters of the heat source

More in detail, for welding pass number 2 and 3, a superposition of two Goldak's heat sources were used in order to better reproduce the weld pool shapes induced of these last two welding runs. Table 4 specifies the different geometrical parameters of the overlapped heat sources used in runs 2 and 3.

Table 3 Goldak's source parameters (Fig. 4). *indicates that the value used depends on the run (see Table 4).

Q*	Power Input (V-I) [W]	*
η	Efficiency	0.95
Q	Absorbed power [W], with $Q=\eta Q^*$	-
a		*
b		*
c_1	Molten pool dimensions [mm]	*
c_2		*
f_1	Constants for the energy distribution of the heat flux	0.6
f_2		1.4
v	Welding speed [mm s ⁻¹]	*
τ	Total duration of time before the welding source has traversed the transverse cross section of the plate [s]	*

Table 4 Geometrical heat source parameters given as a function of the welding pass. Second and third pass were simulated using a superposition of two Goldak's heat sources

Welding pass	a [mm]	b [mm]	c_1 [mm]	c_2 [mm]	τ [s]
1	6	6.5	5.3	10.9	32.7
2(1)	25	0.7	7	15	
2(2)	2.7	2	3.5	7	138.3
3(1)	25	0.7	7	15	
3(3)	3	2	3.5	7	647.36

RESULTS AND DISCUSSION

Microstructure

The HAZ microstructure observed by optical microscope is shown in Fig. 5. Colonies of precipitates were detected within ferrite grains. As shown in Fig. 6, the secondary electron SEM micrograph clearly reveals intragranular precipitates after chemical etching.

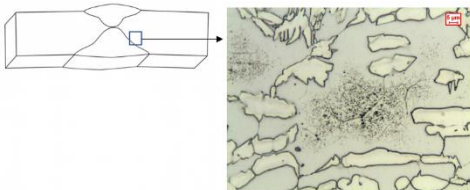


Fig. 5 OM micrograph of HAZ in weld SDSS sample

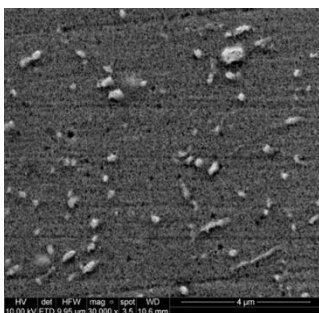


Fig. 6 Secondary electron SEM micrograph of a colony of precipitates within ferrite grain.

Figs. 7a and **7b** show the EDS-linescan image and elemental distribution profiles across the precipitate and the surrounding ferrite grain, respectively. The concentrations of N and Cr are higher within the precipitate as compared to the ferrite matrix while a Fe reduction is observed; in addition, no variations of the C content was observed along the profile excluding carbide particle precipitation. Therefore, neglecting the signal contribution of surrounding α -Fe matrix to the distribution profile, it can be concluded that the precipitate is consistent with a chromium nitride particle.

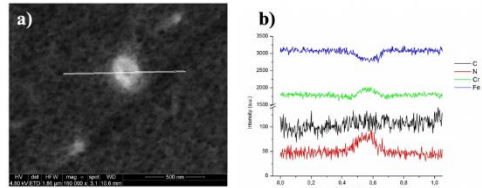


Fig. 7 a) EDS-linescan image and b) corresponding elemental profiles

Fig. 8a shows the morphology of nanometer-sized chromium nitrides at high magnification. As a comparison, in Figs. 8b and 8d TEM micrographs taken from the work of Petterson et al. [32] and Nilsson [18], respectively, are reported. In particular, in Petterson's work chromium nitrides were found to precipitate in a UNS S32750 SDSS cooled from 1225 °C with a cooling rate of 100K/s while Nilsson for the first time identified the rod-shaped precipitates as Cr-N using ED in TEM.

Finally, **Fig. 8c** shows another detail of chromium nitride distribution found in the present alloy. They are observed both inside the ferrite grains and in ferrite sub-grain boundaries.

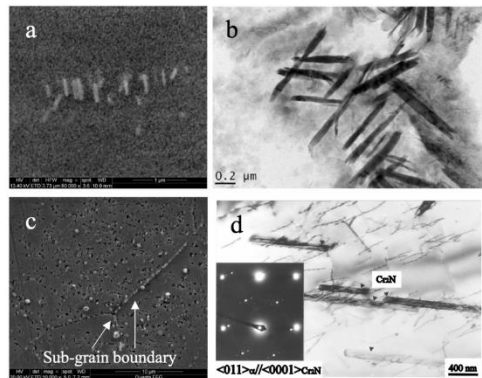


Fig. 8 a) The morphology (a) (b) (d) and distribution (c) of chromium nitrides. Pictures (b) and (d) are TEM micrographs published in ref. [32] and [18], respectively

Finally, the volume fractions of ferrite in FZ, HAZ and PM are summarized in **Fig. 9a**. It was observed that the HAZ shows the highest amount of δ ferrite (59%). This is because of the high cooling rates and the slow diffusion of Ni in the Ni-rich filler metal. Despite the relatively fast diffusion of nitrogen, the cooling rate is so high that nitrogen is unable to escape from the ferrite leading to supersaturation and subsequent Cr-N precipitation, as schematized in **Fig. 1**.



Fig. 9 Microstructure and ferrite proportion in different zones of the weld (a) and micrograph of the HAZ (b)

Numerical results

Fig. 10 shows the shape and dimension of the fusion zone (red colour) obtained by welding simulation. The use of a double heat source function was found successful in capturing the correct FZ shape of beads 2 and 3. The thermal model was used to both characterize the austenite proportion in FZ and estimate the cooling rate promoting precipitation of chromium nitrides in HAZ. In fact, during cooling, in the temperature range 1200 – 800 °C, δ-ferrite partially transforms to primary austenite. The corresponding volume fraction formed at time t (V_f) will depend on the cooling rate according to the relation proposed by Lindblom and Hannerz [33]:

$$V_f = (Dt_{12-8})^m \tag{9}$$

where Δt_{12-8} is the time interval elapsed during cooling from 1200 to 800 °C while m is a parameter that depends on the alloy composition. Using numerical simulation and the measured austenite volume fraction in FZ induced by the last welding pass ($V_f = 0.47$, **Fig. 9**) it was obtained $\Delta t_{12-8} = 24$ s and therefore, from

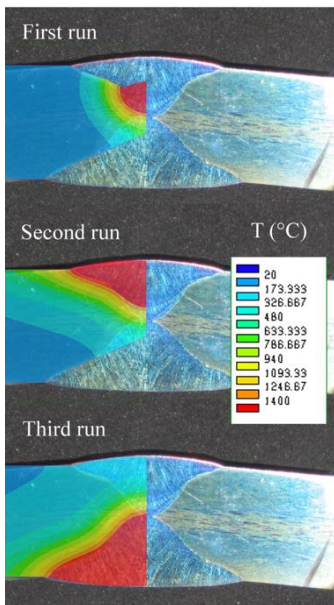


Fig. 10 Temperature maps at the instant of maximum FZ size (red color) as a function of welding pass and comparison with weld bead macrograph.

Eq. (9), $m = -0.237$. In **Fig. 11**, both the temperature evolution and its derivative at a node belonging to the HAZ of the third weld bead are plotted. During cooling, in the temperature interval between 1280 and 900 °C, the cooling rate ranges from -50 °C/s to -20 °C/s, that is in perfect agreement with the cooling rates promoting Cr-N precipitation in the same SDSS (-20÷-100 °C/s) found by Pettersson et al. [32].

The 2D proposed model is therefore proven to be a useful design tool instrument able to capture the conditions under which chromium nitrides may forms. Because of its rapid solution, it can be used to predict the optimal process parameters assuring the lowest risk of secondary phases precipitation.

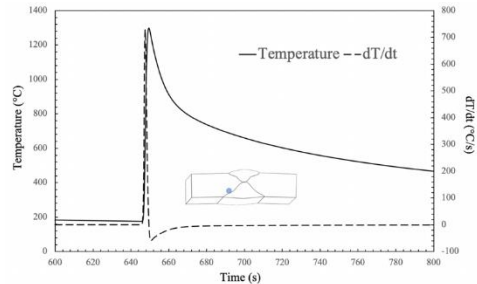


Fig. 9 Temperature and its derivative evolution in HAZ of the third weld bead

CONCLUSIONS

Rapid cooling prevents the formation of intermetallic phases but if the cooling is not properly controlled, there is a risk of forming chromium nitrides in nitrogen-rich DSS and SDSS. Chromium nitrides can promote pitting corrosion and must therefore be avoided. Unfortunately, they are not easily detectable with standard metallographic techniques, because of their sub-micron dimensions. On the other hand, investigations using advanced instruments such as the transmission electron microscope, are time-consuming and, consequently, of limited practical use for industrial application. A methodology aimed at detecting Cr-N in the HAZ of a SDSS using the field-emission gun scanning electron microscope is suggested and presented here. It was found to be more efficient and practical compared to TEM investigations. Finally, a thermal numerical model of the multi-pass welding process was also developed that allows welding engineer to estimate the cooling rates promoting Cr-N precipitation in the HAZ. The results were found to be in excellent agreement with those found in the literature.

REFERENCES

1. S.S.M. Tavares, J.M. Pardal, L.D. Lima, I.N. Bastos, A.M. Nascimento, J.A. de Souza: Materials Characterization, 58, 2007, 610–616. <https://doi.org/10.1016/j.matchar.2006.07.006>.
2. P. Ferro, J.-O. Nilsson, F. Bonollo: Acta Metallurgica Slovaca, 24(2), 2018, 147-155. <https://doi.org/10.12776/ams.v24i2.1073>.
3. R.A. Perren, T. Suter, C. Solenthaler, G. Gullo, P.J. Uggowitzer, H. Bohni, M.O. Speidel: Corrosion Science, 43, 2001, 727-745. [https://doi.org/10.1016/S0010-938X\(00\)00088-3](https://doi.org/10.1016/S0010-938X(00)00088-3).

4. B. Deng, Z. Wang, Y. Jiang, T. Sun, J. Xu, J. Li: Corrosion Science, 51, 2009, 2969–2975.
<https://doi.org/10.1016/j.corsci.2009.08.015>.
5. Y.-L. He, N.-Q. Zhu, X.-G. Lu, L. Li: Materials Science and Engineering A, 528, 2010, 721–729.
<https://doi.org/10.1016/j.msea.2010.09.067>.
6. N. Sathirachinda, R. Pettersson, S. Wessman, J. Pan: Corrosion Science, 52, 2010, 179–186.
<https://doi.org/10.1016/j.corsci.2009.08.057>.
7. R. Cervo, P. Ferro, A. Tiziani: Journal of Materials Science, 45, 2010, 4369–4377.
<https://doi.org/10.1007/s10853-010-4310-1>.
8. R. Cervo, P. Ferro, A. Tiziani, F. Zucchi: Journal of Materials Science, 45, 2010, 4378–4389.
<https://doi.org/10.1007/s10853-010-4311-0>.
9. P. Ferro, F. Bonollo: Metallurgical and Materials Transactions A, 43, 2012, 1109–1116.
<https://doi.org/10.1007/s11661-011-0966-7>.
10. P. Ferro: Acta Materialia, 61, 2013, 3141–3147.
<https://doi.org/10.1016/j.actamat.2013.01.034>.
11. P. Ferro, A. Fabrizi, F. Bonollo: Acta Metallurgica Sinica, 29(9), 2016, 859–868.
<https://doi.org/10.1007/s40195-016-0462-6>.
12. P. Ferro, A. Fabrizi, J.-O. Nilsson: Research and Reports on Metals, 1(2), 2017, 1–6.
13. K. Migiakis, G.D. Papadimitriou: Journal of Materials Science, 44, 2009, 6372–6383.
<https://doi.org/10.1007/s10853-009-3878-9>.
14. T. Ogawa, T. Koseki: Welding Journal, 68(5), 1989, 181s–191s.
15. F. Bonollo, A. Gregori, A. Tiziani, J.-O. Nilsson: A study on microstructural evolution of superduplex steels (SAF 2507) induced by isothermal heat treatment. *Proceedings of 11th congress of the international federation for heat treatment and surface engineering*, Associazione Italiana di Metallurgia, Milano, 3, 1998, 291–300.
16. A. J. Ramirez, S. D. Brandi and J. C. Lippold: Science and Technology of Welding and Joining, 9, 2004, 301–313.
<https://doi.org/10.1179/136217104225021715>.
17. A. Gregori, J.-O. Nilsson: Metallurgical and Materials Transactions A, 33, 2002, 1009–1018.
<https://doi.org/10.1007/s11661-002-0202-6>.
18. J.-O. Nilsson: Materials Science and Technology, 8, 1992, 685–700.
<https://doi.org/10.1179/mst.1992.8.8.685>.
19. S.S.M. Tavares, C. Scandian, J.M. Pardal, T.S. Luz, F.J. da Silva: Engineering Failure Analysis, 17, 2010, 1500–1506.
<https://doi.org/10.1016/j.engfailanal.2010.05.012>.
20. C.M. Garzon, A.J. Ramirez: Acta Materialia, 54, 2006, 3321–3331.
<https://doi.org/10.1016/j.actamat.2006.03.018>.
21. D. Bruch, D. Henes, P. Leibenguth, Ch. Holzappel: La Metallurgia Italiana, 6, 2008, 7–13.
22. A.J. Ramirez, J.C. Lippold, S.D. Brandi: Metallurgical and Materials Transactions A, 34, 2003, 1575–1597.
<https://doi.org/10.1007/s11661-003-0304-9>.
23. Z. Zhang, H. Jing, L. Xu, Y. Han, L. Zhao, J. Zhang: Applied Surface Science, 394, 2017, 297–314.
<https://doi.org/10.1016/j.apsusc.2016.10.047>.
24. H. Tan, Z. Wang, Y. Jiang, Y. Yang, B. Deng, H. Song, J. Li: Corrosion Science, 55, 2012, 368–377.
<https://doi.org/10.1016/j.corsci.2011.10.039>.
25. Y. Shi, S. Cui, T. Zhu, S. Gu, X. Shen: Journal of Materials Processing Technology, 256, 2018, 254–261.
<https://doi.org/10.1016/j.jmatprotec.2018.02.019>.
26. Z. Zhang, Z. Wang, Y. Jiang, H. Tan, D. Han, Y. Guo, J. Li: Corrosion Science, 62, 2012, 42–50.
<https://doi.org/10.1016/j.corsci.2012.04.047>.
27. T.H. Chen, J.R. Yang: Materials Science and Engineering A, 338, 2002, 166–181.
[https://doi.org/10.1016/S0921-5093\(02\)00065-5](https://doi.org/10.1016/S0921-5093(02)00065-5).
28. Ø. Grong: *Metallurgical modelling of welding*. The Institute of Materials, London, Great Britain, 1997.
29. R. Goyal, E. Johnson, M. El-Zein, J. Goldak, M. Coulombe, S. Tchernov: A Model Equation for the Convection Coefficient for Thermal Analysis of Welded Structures. In *Proceedings of the Trends in Welding Research*, Proceedings of the 8th International Conference; Eds. S.A. David, T. DebRoy, J.N. DuPont, T. Koseki, ASM Intl., Ohio, United States; 2008, 321–327.
30. J. Goldak, A. Chakravarti, M. Birby: Metallurgical and Materials Transactions B, 15, 1984, 299–305.
<https://doi.org/10.1007/BF02667333>.
31. P. Ferro, F. Bonollo, A. Tiziani: International Journal of Computational Materials Science and Surface Engineering, 3, 2010, 114–132.
<https://doi.org/10.1504/IJCSSE.2010.033148>.
32. N. Pettersson, R.F.A. Pettersson, S. Wessman: Metallurgical and Materials Transactions A, 46, 2015, 1062–1072.
<https://doi.org/10.1007/s11661-014-2718-y>.
33. J. C. Lippold, D. J. Kotecki: *Welding Metallurgy and Weldability of Stainless Steels*, Wiley-VCH, Hoboken, New Jersey, 2005.